Universal Journal of Lasers, Optics, Photonics & Sensors (UJLOPS)
UINUJLOPS202308/W. Arrasmith[1], E. He[2]

Application of the Well-Optimized Linear Finder (WOLF) Atmospheric Turbulence Compensation Method to Hyperspectral Imaging Systems

W. Arrasmith[1], E. He[2]
[1]Florida Institute of Technology, Melbourne, FL, USA warrasmi@fit.edu, 321-674-8818
[2]Florida Institute of Technology, Melbourne, FL, USA ehe@fit.edu

ABSTRACT

The Well-Optimized Linear Finder (WOLF) high-speed transfer function estimation method has been shown to apply to diversity-based imaging systems for atmospheric turbulence compensation (ATC) purposes. Thus far, the WOLF methodology has been applied to only monochromatic imaging systems with the understanding that the extension to colored imagery such as those that use the RGB color cube (or some other color mapping scheme) are straight forward once the ATC is accomplished at a single wavelength. In this work, we investigate the application of the WOLF algorithm to hyperspectral imaging (HSI) systems and show that there is a benefit not only to the achievable spatial resolution of the HSI system at any given wavelength, but also a benefit to the achievable per-pixel signal-to-noise ratio (SNR) across all wavelengths where a detectable amount of signal is present. In the latter case, the increase in the per-pixel SNR will permit better discrimination of spectral signatures. A notional conceptual optical layout is presented to provide a platform agnostic means to illustrate our approach. The use of a representative variable entrance pupil plane mask, such as can be achieved with the employment of a spatial light modulator (SLM) or rotating reticle, can be used in concert with the WOLF algorithm to generate high-speed ATC results for HSI imagery. The benefits of using the SLM to imprint a known entrance pupil plane phase offset in the detected HSI imagery is also presented. An example of the WOLF methodology applied to a "push-broom" HSI system is given for a diversity-based imaging system, along with a platform agnostic speed comparison of the WOLF with representative traditional ATC methods.

INTRODUCTION

In well-designed optical imaging systems that are looking through the Earth's atmosphere, the imaging system can experience a dramatic loss in spatial resolution if the entrance pupil plane diameter of the optical system is larger than the atmospheric coherence length (Fried parameter) ro.[1] The larger the entrance pupil plane diameter (e.g., the primary mirror diameter on a telescopic imaging system) is with respect to ro, the larger the loss of spatial resolution due to atmospheric turbulence effects.[2] These atmospheric turbulence effects on the performance of the imaging system occur regardless of how well the imaging system is designed and are present even if a "perfect" aberration-free imaging system where possible and present, and thereby constitute the limiting effects on the imaging system's achievable spatial resolution. To mitigate the effects of atmospheric aberrations on atmosphere-bound imaging systems, and attempt to restore the capability to provide diffraction-limited spatial resolution in the collected imagery, either adaptive optics (AO), atmospheric turbulence compensation, or hybrid methods are generally used.[3] AO systems are typically hardware-based and are real-time capable (faster than 30 Hz), complex, bulky, not generally mobile, relatively expensive, and often require precise alignment and calibration.[4,5] ATC methods are software dominant but traditionally slow when compared to AO systems and so are most often used in post-processing applications. Hybrid methods are a combination of AO and

ATC methods and their performance falls somewhere in between the AO and ATC performance capabilities (e.g., not as bulky as AO systems but more bulky than ATC systems, faster than traditional ATC imaging systems, but not as fast as AO systems, and so forth). Recently, the Well-Optimized Linear Finder (WOLF) methodology developed by William Arrasmith was shown to provide a software-dominant, real-time scalable ATC capability, that can provide diffraction limited spatial resolution on diversity-based imaging systems using only the diversity-based image pair and a laptop computer.[6] It was demonstrated that the WOLF methodology could remove the atmospheric turbulence from a 256 by 256 pixel image segment in approximately 9 seconds on a 2014 MacBook Pro laptop computer without any optimization and without using a General Purpose Parallel Processor (GPPP).[7] Complexity analysis studies showed that with the use of a GPPP, the WOLF methodology could be implemented in real-time (remove the atmospheric turbulence faster than 30 Hz) and have potential applicability to video streams as well as single images.[8] To date the WOLF methodology has been applied to single wavelength (grayscale) imaging systems. In this paper, we extend the WOLF algorithm to hyperspectral imaging systems and present a notional implementation concept that could benefit both the HSI system's ability to provide higher spatial-resolution images and provide a higher per-pixel signal-to noise ratio (SNR) allowing for better spectral discrimination.

ANALYSIS

HSI systems come in a variety of shapes and types. Figure 1 below notionally shows several different types of HSI systems that currently exist and are conventionally deployed using a variety of implementation methods. The x and y axes represent the spatial orientation in which the WOLF methodology can be applied to single wavelength images to perform ATC resulting in high spatial-resolution images for the x - y spatial array of pixels. The different images in Figure 1 show different HSI implementation methods to achieve the

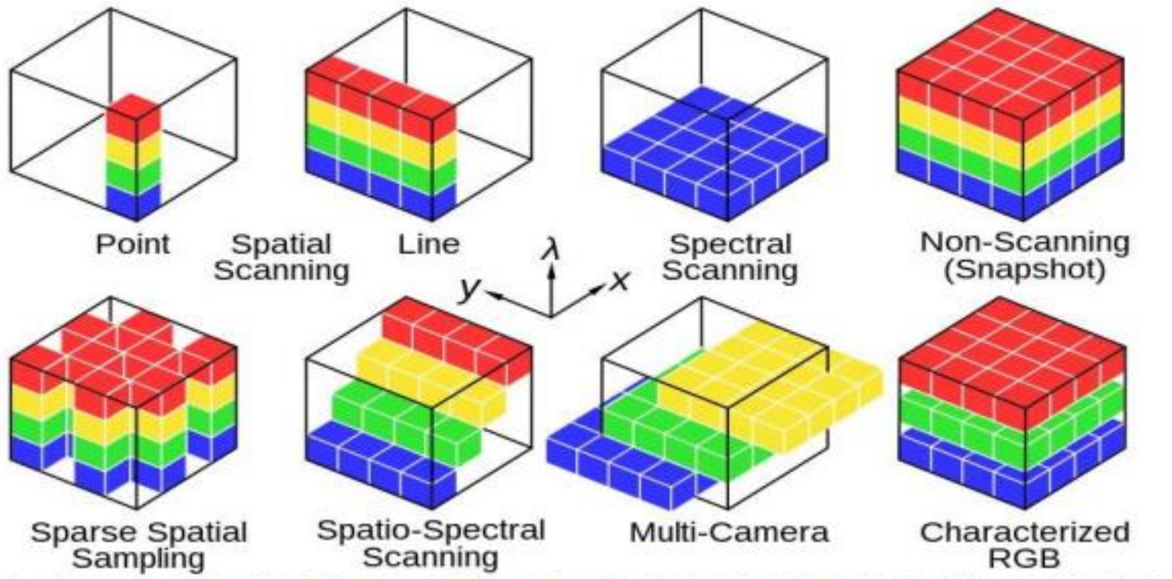

Figure 1 – Various Hyperspectral Imaging system implementation approaches [9]

so-called hyperspectral data cube that consists of the 2D spatial data (horizontal plane) along with the vertical plane of wavelength data. Note that in Figure 1, only 4 different wavelengths are shown as representatives of the different wavelengths (or spectral bands). There can be hundreds of wavelengths (spectral bands) collected with the hyperspectral imaging system. In one implementation of the WOLF methodology applied to HSI systems, there must be equal to, or more wavelengths available than half the entrance pupil plane sample points in a linear direction for the

WOLF ATC method to make use of the entrance pupil plane mask method described below. Other implementations of the WOLF ATC method can be employed that require only 2 separate wavelengths but require shorter integration times at each wavelength or have HSI implementations that provide separable spatial frequency information simultaneously at two wavelengths such as a line scanner that provides linear array spatial and/or spatial frequency information simultaneously at two wavelengths. However, if it is not possible to have more wavelengths than half the entrance pupil plane samples in a linear direction for the image segment being corrected (such as in multi-spectral imaging systems or colored video), then the WOLF methodology can still be applied without employing the entrance pupil plane mask, but using conventional methods as detailed below, albeit at slower speeds than is possible with the entrance pupil plane aperture mask present. In Figure 1, the top-left graph indicates a “point-sensor” such as a single pixel being used with multiple wavelengths being simultaneously collected at the same pixel spatial location. This type of HSI sensor would produce a vector of different irradiance values for the same pixel at different wavelengths (or spectral bands). This single pixel would be scanned through the x – y spatial array to map out the spatial image irradiance values along with the corresponding wavelength data associated with each spatial pixel location. The second from top-left image corresponds to a “line scanner” which uses a linear array (vector) of pixels to simultaneously map out one spatial direction of the image (y – direction above) and simultaneously collect the wavelength (spectral) data associated with each pixel. These types of sensors are typically employed in a “push broom” mode (the linear array is “pushed” in the x – direction which is the same direction of movement as the sensor platform motion), or in a “whiskbroom” mode (the sensor platform is moving in the y - direction with the linear array “whisked” back and forth in the x – direction). The third image from the top-left shows a conventional imaging system captured at one wavelength and produces a grayscale image. The last image on the top row shows a hyperspectral image cube that simultaneously captures both image data and wavelength (spectral) data. The bottom row shows other HSI collection modalities such as sparse aperture (bottom left), step-stair (bottom, second from left), multi-camera (second from bottom right), and RGB. In the last mode, the RGB color cube is used to reconstruct a colored image. The WOLF methodology will work with all these implementations but for clarity’s sake, we focus on the “push broom” HSI mode as shown in the second from the top-left image. As stated, this mode provides a linear array of spatial pixels along with image irradiance values at each wavelength that are simultaneously captured. There are a variety of physical mechanisms for producing this HSI data set using combinations of optical elements such as lenses, collimators, gratings, prisms, and rotating mechanisms, however, we focus on a general conceptual implementation to illustrate the fundamental concepts of the WOLF methodology, and consequently ignore HSI implementation specific details.[10,11] Before discussing the WOLF ATC methodology using the HSI push broom implementation discussed above, we need to develop a notional diversity based HSI conceptual model that features the general attributes required to generate a pair of HSI diversity images that serve as inputs to the WOLF algorithm. Figure 2 provides this notional conceptual model. In the upper left, we see an object that is being imaged by theHSI system in Figure 2. The optical radiant emittance reflected from the natural light illuminated far-field object (satellite figure), propagates through the atmosphere, and is intercepted by a primary mirror located in the entrance pupil plane of the imaging system (EPM). The collected irradiance is collimated using the collimator at C1 and the slit at S1 separates one line of pixels from the 2D spatial frequency array. Part of the collimated light is redirected upwards at Beam Splitter 1 (BS1) and the prism at P2 separates out the wavelengths in the horizontal direction. The orientation of the irradiance at the Spatial Light Modulator (SLM) is such that the linear array of spatial pixels is oriented out of the page (as indicated by the symbol of the dot inside a circle), and the wavelengths are separated out in the horizontal direction (as shown by the arrow above the SLM). The SLM can be used to imprint an entrance pupil plane mask (e.g., zeros or ones) on the spatial frequency and wavelength components of the array, effectively passing or blocking data from individual spatial frequency sample cells and individual wavelengths as will be seen below. If desired, the SLM can also be used to imprint a known phase off-set at desired grid points of the entrance pupil. This is especially useful in creating a diversity image that has a known entrance pupil pane phase offset with respect to the unknown entrance pupil plane phases induced by atmospheric turbulence effects. The diversity image is needed by diversity-based ATC methods such as the current implementation of the WOLF methodology. For the entrance pupil plane cell blocking application, if a spatial light modulator is not available, then a fixed aperture mask can be created using a reflective mirror (at the SLM) with blocking elements placed at desired pixels and wavelength cells. To turn this blocking pattern on and off, a rotating reticle with the aperture mask

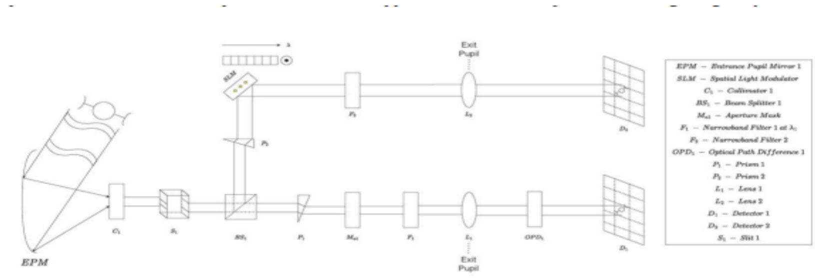

Figure 2 – Conceptual model for diversity based HSI system.

pattern can be employed. The reflected light from the SLM goes through a narrow-band filter L2 capable of selecting any wavelength in the HSI system, or passing all the wavelengths of light. After the narrow-band filter, the electromagnetic wave proceeds through the lens L2 in the exit pupil plane of the imaging system and generates the wavelength filtered irradiance pattern on the detector D2 in the image plane of the optical system. The other part of the electromagnetic wave that passes through the beam splitter at BS1 goes through a similar prism P1, followed by a transmissive aperture mask Ma1 that is identical to the aperture mask at the SLM (and can also be selectively turned on or off), and a selectable narrow-band filter that can be used to select any specific HSI system wavelength of the irradiance spectrum, or pass all the wavelengths of the irradiance spectrum if desired. The filtered light at F1 goes through the lens L1 that is located at the imaging system's exit pupil. The Optical Path Difference block at OPD1 adds a slight delay between the electromagnetic waves in the separate optical paths and results in a defocus phase effect in the entrance pupil plane. The addition of the entrance pupil plane defocus effect can be used to generate the diversity image needed by the diversity-based atmospheric turbulence compensation element (in our case implemented by the WOLF ATC algorithm). The known phase offset (defocus term) in the entrance pupil plane of the imaging system can then either be added by the Spatial Light Modulator, or by the optical path difference block OPD1.

We now show how the notional optical layout shown in Figure 2 can be used in conjunction with the WOLF methodology to remove atmospheric turbulence from the captured HSI imagery. We start with explaining the purpose and utility of the entrance pupil plane aperture mask by employing a specific mask implementation. We use an aperture mask pattern at the SLM that has the benefit of 1) requiring only a 1- point overlap WOLF algorithm to be used to remove the atmospheric aberrations from any required point of the image. The WOLF 1-point overlap algorithm is the fastest algorithm in the WOLF ATC methodology and so provides a direct processing speed benefit by not requiring the WOLF 2-point overlap, or WOLF 3- point (or more) algorithm which are more computationally complex, and generally much slower than the WOLF 1-point algorithm. The second benefit of the aperture mask shown below is that it allows each of the wavelengths to be independently processed. This provides a huge speed increase potential which will be quantified below. Figure 3 shows the entrance pupil plane irradiance spectrum array after the specific aperture mask has been applied (left side) at the spatial light modulator (SLM). The orientation of the map has been rotated so that the spatial frequency sample points of the linear push broom array are shown on the horizontal axis, and the wavelength components are shown in the vertical direction from top to bottom. In this fashion the first pixel of the spatial array at the first wavelength ($\lambda 1$) is shown at the top left of the array and is consistent with the array structure in MatlabTM. This is convenient for application and subsequent processing of the WOLF methodology to the resulting masked irradiance spectrum to estimate and remove the atmospheric turbulence from the imagery. The figure on the left shows an entrance pupil plane aperture mask where the gray areas show irradiance spectrum cells in the array that are zeroed out (the mask is applied at those locations), and the clear areas show cells that return the actual irradiance spectrum values at that cell location (no effect of the mask in clear cells). For instance, the top row in the left side of Figure 3 shows all clear cells and so contains the original irradiance spectrum values for each cell of the original push broom linear spatial array at $\lambda 1$. One way to think about the effect of the entrance pupil plane mask is to consider the white open areas as mirror reflection points where the electromagnetic wave is preserved and reflected and the dark areas zero out the electromagnetic field contribution at that location. The grid on the right side of Figure 3 shows the grid cell structure (all white) when the mask is turned off. In this case, all the electromagnetic field components are reflected and preserved, and, dependent on the object spectrum and optical transfer function element at the coincident spatial frequency location. Consequently, it is possible to have complex irradiance spectrum values in some, or all the white cells shown in the grid of cells in the right side of Figure 3. We next develop the mathematical framework to illustrate the advantages of incorporating this entrance pupil plane mask in removing atmospheric turbulence from collected HSI images using the diversity-based imaging concepts.

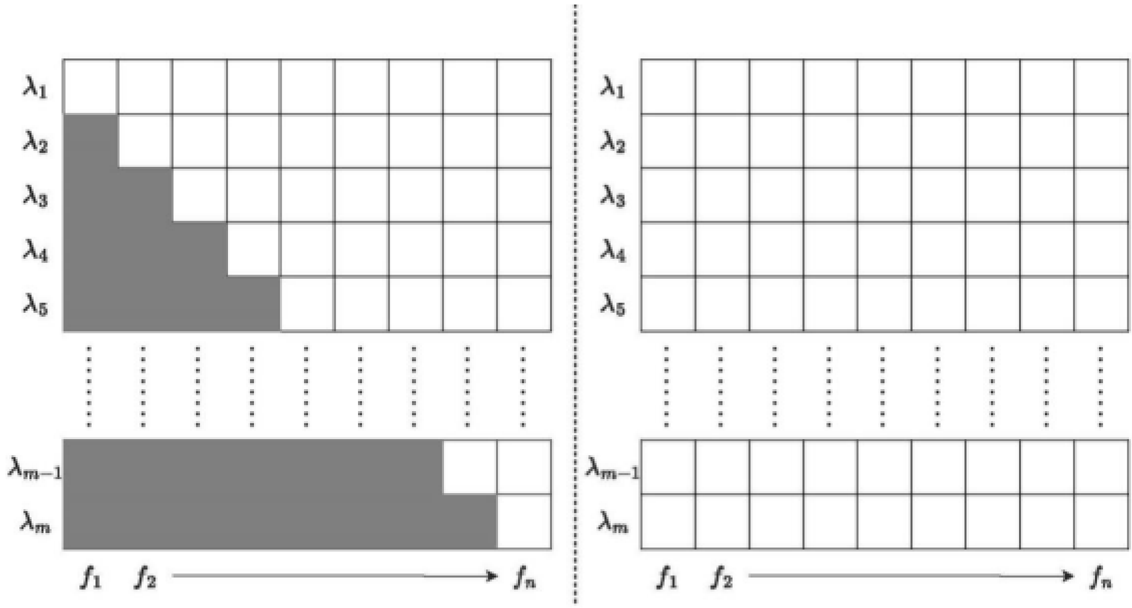

Figure 3 – Entrance pupil plane mask for HSI system.

Since we assume that the entrance pupil of the HSI system is in the far-field of the object, and the object maximum spatial extent is small compared to the separation distance between the object and the entrance pupil of the imaging system, we can use linear systems theory to provide the mathematical framework to solve the ATC problem and apply these constructs to HSI systems.[12,13] For general linear, shift-invariant systems, we can relate the image irradiance spectrum at a given wavelength to the object radiant emittance spectrum by,

$$I^{\lambda_n}(\vec{f}) = O^{\lambda_n}(\vec{f})\mathcal{H}^{\lambda_n}(\vec{f}), \tag{1}$$

where $O^{\lambda_n}(\vec{f})$ is the object radiant emittance spectrum at center wavelength λ_n and spatial frequency $\vec{f} = (f_y, f_x)$, $\mathcal{H}^{\lambda_n}(\vec{f})$ is the Optical Transfer Function (OTF) at the same wavelength and spatial frequency location, and $I^{\lambda_n}(\vec{f})$ is the image irradiance spectrum, again at the same spatial frequency and center wavelength. It can be seen from Equation (1) that if we can estimate the OTF at the given wavelength and spatial frequency, then we can invert the OTF and determine the pristine atmospheric turbulence free object radiant emittance. We will use the WOLF methodology to estimate the OTF at the required spatial frequency locations to fully reconstruct the pristine object radiant emittance spectrum. However, we first need to develop an expression for the OTF in terms of determinable entrance pupil plane parameters. Notice that Equation (1) is in terms of spatial frequency and wavelength parameters and is not explicitly a function of time. This is because we are using Taylor's frozen flow approximation that states that the spatial correlation properties of the atmosphere vary on the order of a few milliseconds. Consequently, to freeze the atmospheric conditions and measure a so-called frozen (in time) state of the atmosphere, our sensor integration times cannot exceed a few milliseconds. The implications on the notional layout that we showed in Figure 2 is that the sensor integration times with the entrance pupil plane mask in the "on" condition should be less than or equal to 1 ms, and the sensor integration time for the mask in the "off" condition should also have a maximum of 1 ms to ensure that the same atmospheric conditions apply to both the mask on and mask off sensor readings. Additionally, we are assuming a single aperture HSI imaging system and so are only interested in spatial and spatial frequency effects, and not temporal effects on the image. The OTF can be related to the Generalized Pupil Function (GPF), $W^{\lambda_n}(\vec{f})$ by,

$$\mathcal{H}^{\lambda_n}(\vec{f}) = \frac{W^{\lambda_n}(\vec{f}) \otimes W^{\lambda_n}(\vec{f})}{N_{ep}}, \tag{2}$$

where N_{ep} is the number of sample points in the entrance pupil plane of the HSI imaging system, and the symbol ⊗ represents 2D autocorrelation. The GPF is given by,

$$W^{\lambda_n}(\vec{f}) = A(\vec{f})e^{j\theta^{\lambda_n}(\vec{f})}, \tag{3}$$

where $A(\vec{f})$ is an amplitude function which is often set to one inside the clear aperture of the entrance pupil and zero outside of the aperture for many imaging system applications for entrance pupils within the Earth's atmosphere (such as Earthbound telescopic imaging systems for instance where near-field turbulence approximations apply). Usually, these amplitude effects may become a factor with laser imaging systems, strong distributed turbulence conditions, or imaging systems with strong scintillation effects. The phase $\theta\ \lambda n(\vec{f})$ is the entrance pupil plane phase due to atmospheric aberrations. We make the often-true assumption that the atmospheric aberrations are dominated by atmospheric phase effects and so set the amplitude value in Equation (3) to one everywhere within the clear aperture of the imaging system. We have also assumed unit magnification. The scaling between spatial coordinates in the entrance pupil and spatial frequency coordinates is given by, $\vec{x} = \lambda n d i \vec{f}$ where di is the imaging system's effective focal length. By substituting Equation (3) into Equation (2) we see that the OTF can be represented by a normalized 2D autocorrelation of the GPF. Traditionally, determining the OTF in this manner is more time intensive than using traditional Fourier-based methods, however, the WOLF methodology has made several advancements where this is no longer true. Specifically, the WOLF methodology has 1) reduced the requirement to calculate possibly millions of complex exponential phase difference sums that are the consequence of performing the 2D spatial autocorrelation of the GPF in Equation (2) to no more than the sum of 2 complex exponentials and a complex constant which can be determined in parallel using a General Purpose Parallel Processor (GPPP), 2) takes advantage of entrance pupil plane phase redundancies in the OTF estimation process, 3) takes advantage of OTF symmetries, 4) accommodates parallel processing implementation methods, and 5) employs optimization strategies for minimizing the computational complexity of the WOLF algorithm, and maximizing the computational speed of the ATC process. Because of these improvements, the WOLF methodology provides a scalable real-time solution for atmospheric turbulence compensation that can be directly extended to HSI imaging sensors. The benefit of the entrance pupil plane aperture mask is to further reduce the computational complexity of the WOLF algorithms as is seen below. Equation (2) shows that the masked OTF after reflecting off the SLM can be determined by a normalized 2D autocorrelation of the GPF. Figure (4) shows one instantiation of this autocorrelation wherein the entrance pupil plane GPF values at each grid point of the fixed entrance pupil plane grid (solid dots) are copied, complex conjugated, and then shifted to the left so that only the first column of the fixed entrance pupil plane GPF values and the last column of the complex conjugated entrance pupil plane GPF values of the moving array (open circles) overlap. This can be seen by the overlapping dots and circles in the center of Figure 4. Notice that we are showing an instance of the graphical 2D autocorrelation of a square entrance pupil plane sampled aperture. We use a square aperture because any other type of aperture can be inscribed within the bounds of the square by zeroing out selected points within the aperture. For instance, a circular aperture can be made from the general square aperture by zeroing points in the corners that are greater than the radius formed by half the longitudinal diameter of the confining square. We use a simple 7 x 7 entrance pupil plane square aperture to illustrate the concepts for the WOLF methodology, but our process and results apply to arbitrarily large entrance pupil plane grid sizes. The coordinate system used in our mathematical representation for a push broom linear spatial array is that the fixed entrance pupil plane grid has its first point at the top-left of the grid. We assign the entrance pupil plane phase associated with this grid point as $\theta i\ \lambda 1$ and the phase at the last point of the spatial component of the fixed array (top right) as $\theta j\ \lambda 1$. The fixed linear array grid coordinate progression goes from left to right with $\boldsymbol{m}\lambda n$ representing the complete set of indices in the linear spatial array, $\boldsymbol{m}\lambda n$ = {1, 2, 3, 4, 5, 6, 7} for the example in Figure (4). A specific column entry value is given by the variable $m\lambda n$ and the maximum index value is $M\lambda n$ = 7 for the example fixed matrix in Figure 4. For example, for the first row with a wavelength of $\lambda 1$, the index value $m\lambda 1$=1 corresponds to the left-most point in the horizontal spatial pixel vector associated with $\lambda 1$ and points to the fixed grid coordinate with phase $\theta i\ \lambda 1$ and GPF value of $e\ j\theta i\ \lambda 1$. Similarly, the moving array can have the spatial linear array index given by a set $\boldsymbol{k}\ \lambda n$ that contains the collective indices for the moving array, $\boldsymbol{k}\ \lambda n$ = {1, 2, 3, 4, 5, 6, 7}. In the same manner, for each other row of wavelengths, the left-most point is represented by $\theta i\ \lambda n$ and the right-most point by $\theta j\ \lambda n$. The shifted, mobile entrance pupil plane grid shown by the circles in Figure 4 contains the complex conjugated copy of the fixed array values, and so the GPF phase of the moving grid values are the exact negatives of those of the fixed grid values. For example, the left-most GPF value of the moving array is given by $e\ -j\theta i\ \lambda n$, and the right-most GPF value of the moving array is given by $e\ -j\theta j\ \lambda 1$

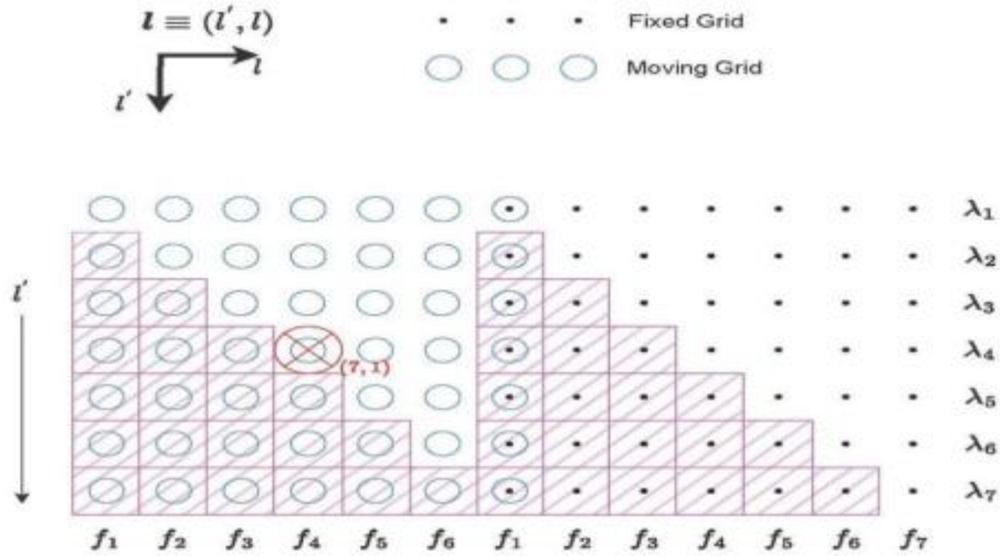

Figure 4 – Optical Transfer Function at spatial frequency coordinate l = (7, 1).

The OTF value at the spatial frequency indicated by the circled X at the center of the moving array is then just the product of the fixed grid GPF with the moving grid, complex conjugated GPF, with individual resulting terms summed together, and normalized by dividing the result by the total number of entrance pupil plane samples, Nep. Notice that in the masked autocorrelation instance shown in Figure 4, the gray overlapping areas are zeroed out because of the aperture mask leaving only the top term in the column of overlapping grids to contribute to the OTF. The resulting OTF is then given by, $\mathcal{H}\lambda1\ (l7,f1\ ) = e\ j\Delta\theta i,j\ \lambda1\ /Nep$. Note that the coordinates on the spatial frequencies are associated with the grid index for the OTF itself. The OTF grid index is given by the matrix l = (l′, l) where l′ runs in the top to bottom direction (over the wavelengths), and l runs from left to right (over the spatial frequencies), with maximum values of (L′, L). The OTF is the normalized 2D autocorrelation of the GPF and so, for N distinct wavelengths in the HSI system has dimensions of (2N-1, 2M-1). For the example shown in Figure 4, we have 7 spatial frequency samples in the horizontal direction and 7 different wavelengths in the top-down vertical direction resulting in dimensions of (13, 13) and 169 unique OTF cells (paired wavelength, spatial frequency samples). Using the OTF coordinate system, the red center X that marks the location in Figure (4) indicates where the OTF is being represented/calculated and has l coordinates of (7,1) meaning that the OTF is being determined in the 7 th row and 1st column of the larger l grid. Note that for a l = (1,1) 1-point overlap condition, the moving array has moved as far to the left, and upwards as possible for a non-zero overlap condition, such that there is only a 1-point overlap between the bottom right corner of the moving grid, and the top left corner of the fixed grid. Any further shift leftwards or upwards of the moving grid results in no overlap and a value of zero for the OTF at that location. Also, the image irradiance spectrum $I\ \lambda n(\vec{f})$ and the object radiant emittance spectrum $O\ \lambda n(\vec{f})$ share the same l – index grid as the OTF. We now have enough information and mathematical formalism to understand the advantage of employing the entrance pupil plane mask and illustrate how the WOLF methodology is used to efficiently remove the atmospheric turbulence from the collected HSI imagery. We previously mentioned that the l – grid has 13 by 13 cells for the 7 by 7 entrance pupil plane grid structure shown in Figure 4. Conventionally, this would require the OTF to be determined at 169 individual cells to fully reconstruct the OTF for all spatial frequencies and wavelengths. By employing the entrance pupil plane mask shown on the left side of Figure 3, we only need to estimate OTF values that align horizontally (spatially) and at the same wavelength as shown in Figure

4. Further, only (M + 1)/2 individual OTF values need to be estimated to fully reconstruct the OTF at all relevant wavelengths. For the example in Figure 4, this results in only 4 required estimates of the OTF instead of the possible 169 values resulting in a remarkable reduction in computational complexity using the entrance pupil plane mask approach shown in Figure 4. We now illustrate how the WOLF methodology can be used in conjunction with this entrance pupil plane mask approach to provide these remarkable results.

Figure 4 shows that the mathematical representation of the OTF at the $\boldsymbol{l}$ – grid coordinate (7,1) is given by,

$$\mathcal{H}^{\lambda_1}(l_7, f_1) = e^{j\Delta\theta_{i,j}^{\lambda_1}} / N_{ep} \, , \tag{4}$$

where $\Delta\theta_{i,j}^{\lambda_1} = \theta_i^{\lambda_1} - \theta_j^{\lambda_1}$, which are the left-most and right-most entrance pupil plane atmospheric phase aberrations of the top-most linear spatial array. From Equation (1), we see that,

$$I^{\lambda_1}(l_7, f_1) = O^{\lambda_1}(l_7, f_1)\mathcal{H}^{\lambda_1}(l, f_1), \tag{5}$$

And the $\boldsymbol{l}$ – grid coordinates for the OTF, object radiant emittance spectrum, and image spectrum are co-located. We can get the complex value of the irradiance spectrum at $\boldsymbol{l}$ = (7,1) by taking the 2D Fourier transform of the detected image at detector D_1 in Figure 2, with the aperture mask on, and looking at the irradiance spectrum at the $\boldsymbol{l}$ – grid coordinate (7,1). Since we are using a diversity-based imaging system, we can introduce a slight defocus term in the entrance pupil plane phase values by adjusting the optical path to detector D_2 using the Optical Path Difference block in Figure 2. The wavelength filters F_1 and F_2 do not matter yet since there is only one wavelength contributing to the OTF shown in Equation (4) due to the SLM employing the entrance pupil plane mask. For the overlap scenario shown in Figure 4, these narrow-band filters can be set to all-pass, or to λ_1 with equal effect. The transmissive entrance pupil plane mask M_{a1} should be set to match the entrance pupil plane aperture mask at the *SLM* shown in Figure 4. The OTF for the diversity irradiance spectrum can then be mathematically expressed as,

$$\mathcal{H}_d^{\lambda_1}(l_7, f_1) = e^{j\left(\Delta\theta_{i,j}^{\lambda_1} + \Delta\theta_{d:i,j}^{\lambda_1}\right)} / N_{ep} \, , \tag{6}$$

where $\Delta\theta_{d:i,j}^{\lambda_1} = \theta_{d:i}^{\lambda_1} - \theta_{d:j}^{\lambda_1}$ can be determined numerically in advance based on the optical path difference between the beam splitter BS_1 and detectors D_1 and D_2. For the diversity irradiance spectrum, we get from Equation (1),

$$I_d^{\lambda_1}(l_7, f_1) = O^{\lambda_1}(f_7, f_1)\mathcal{H}_d^{\lambda_1}(f_7, f_1) \, , \tag{7}$$

where once again, the left side of Equation (7) can be directly measured from the 2D Fourier Transform of the irradiance measured at detector D_2. At this point, we can make an interesting observation by writing the object spectrum in its phasor form and combining the result with the explicit expression of the OTF in Equation (5). The result is,

$$I^{\lambda_1}(l_7, f_1) = \left|O^{\lambda_1}(l_7, f_1)\right| e^{j\left(\phi_o^{\lambda_1}(l_7, f_1) + \Delta\theta_{i,j}^{\lambda_1}\right)} / N_{ep} \, , \tag{8}$$

where $\emptyset o\ \lambda 1\ (l7,\ f1\ )$ is the object radiant emittance spectrum phase at l – grid coordinate (7, 1). Notice that if we take the absolute value of the measured irradiance spectrum at the l – grid coordinate (7,1), then we directly recover the object radiant emittance spectrum magnitude divided by the known number of entrance pupil sample points, Nep. This interesting feature works for all 1-point overlap scenarios in our approach, and at all wavelengths. We now need to determine the corresponding object radiant emittance spectrum phase $\emptyset o\ \lambda 1\ (l7,\ f1\ )$ to recover the un-aberrated object information (magnitude and phase) for this 1-point overlap scenario. The WOLF methodology accomplishes this by minimizing an appropriate error metric such as the general Gonsalves error metric [14,15,16] given by,

$$E^{\lambda_n}(\vec{f}) = \frac{\left| I^{\lambda_n}(\vec{f})\hat{\mathcal{H}}_d^{\lambda_n}(\vec{f}) - I_d^{\lambda_n}(\vec{f})\hat{\mathcal{H}}^{\lambda_n}(\vec{f}) \right|^2}{\left|\hat{\mathcal{H}}^{\lambda_n}(\vec{f})\right|^2 + \left|\hat{\mathcal{H}}_d^{\lambda_n}(\vec{f})\right|^2}. \quad (9)$$

In Equation (7), we see that the ^ symbol represents an estimate of the quantity underneath (in this case the OTF and the diversity OTF). We also see that this error equation applies to a point estimate at spatial frequency $\vec{f}$ and so is applicable to the spatial frequency at $\boldsymbol{I}$ – coordinate (7,1) in our example shown in Figure 4. We also see that this error metric is only a function of the measured irradiance spectrum values at $\boldsymbol{I}$ – coordinate (7,1) and the estimates for the OTF and diversity OTF for which we have analytical expression in Equations (4) and (6). Further since we are assuming a single aperture HSI system that has only one primary entrance pupil plane collecting aperture, we are concerned only with relative phase effects, and not absolute phase effects, and so are free to choose the initial value of $\theta_i^{\lambda_1}$. Upon inspecting Equation (9) with the substituted values of the OTF and diversity OTF, we see that the only unknown in the error metric is the entrance pupil plane phase $\theta_j^{\lambda_1}$. The WOLF 1-point overlap algorithm (WOLF-Tau) minimizes this error metric and solves for the unknown entrance pupil phase $\theta_j^{\lambda_1}$. This appears to be straightforward by parameterizing $\theta_j^{\lambda_1}$ in the OTF and diversity expressions between the values [-π, π), calculating the error metric in Equation (9), and keeping the value $\theta_j^{\lambda_1}$that belongs to the minimum value of the error metric. However, an additional processing step is required, since for the 1-point overlap condition only, this well-publicized error metric goes to zero for all estimated values of $\theta_j^{\lambda_1}$. Why? The reason is because for the 1-point overlap case, the phase terms within the error metric cancel each other out exactly for all estimates of $\theta_j^{\lambda_1}$. The WOLF-Tau algorithm solves this issue by using a virtual point method to introduce a known phase variation into the phase and amplitude parts of the OTF and diversity OTF, so that the error metric in Equation (7) converges.[11] Also, since these measurements are taken at the edge of the OTF and diversity OTF where the Signal-to-Noise (SNR) may be low, a well-designed imaging system is required to keep the optical system noise as low as possible. Once $\theta_j^{\lambda_1}$is determined by the WOLF-Tau 1-point overlap algorithm, we can determine the atmospheric phase effects at all the wavelengths in the HSI system's entrance pupil plane last column shown in Figures 3 and 4 by,

$$\lambda_1\theta_j^{\lambda_1} = \lambda_n\theta_j^{\lambda_n}. \quad (10)$$

Notice, that the same thing can be accomplished with our guess of $\theta i\ \lambda 1$ at the left-most position of the entrance pupil plane linear spatial array. We can use Equation (10) to convert our chosen phase value of $\theta i\ \lambda 1$ at any wavelength in the first entrance pupil plane column. Since we selected $\theta i\ \lambda 1$ and estimated $\theta j\ \lambda 1$ using the WOLF methodology, we can determine the OTF and diversity OTF in accordance with Equations (4) and (6) and recover the object radiant emittance spectrum phase upon substitution into Equation (8). Since the wavelength scaling in Equation (10) can be used to determine the OTF component at any wavelengths in Column 1 of the entrance pupil, the un-aberrated object radiant emittance spectrum can be directly determined from Equation (1). At this point, we know $\theta i\ \lambda n$ and $\theta j\ \lambda n$ for all wavelengths in the entrance pupil, the OTF and diversity OTF at every wavelength corresponding to the first and last column overlaps of the fixed and moving array GPFs, and the corresponding ATC object radiant emittance spectrum at all wavelengths in accordance with our determined OTFs and Equation (1). If instead corrections are desired on the entrance pupil plane phases at all wavelengths, then this can be accomplished by either directly using the SLM (by negating the entrance pupil plane phases at each wavelength), or by applying wavelength filters to obtain the isolated irradiance spectrum measurement for each wavelength component and dividing by the corresponding OTF component at that wavelength. The entrance pupil plane phase correction likely is not necessary and determining the OTF at all required wavelengths should be sufficient to reconstruct the ATC object spectrum where needed. We have determined all the necessary information for correcting the turbulence degraded imagery resulting from the first and last columns of the entrance pupil plane, along with determining the associated entrance pupil plane phases due to the atmospheric aberrations. We now need to apply the WOLF methodology to the second column of the entrance pupil plane to recover similar information as for the first column 1 – point overlap. Figure 5 shows the 2 – point overlap scenario that is obtained by shifting the moving grid shown in Figure 4 one unit to the right. We see that there are

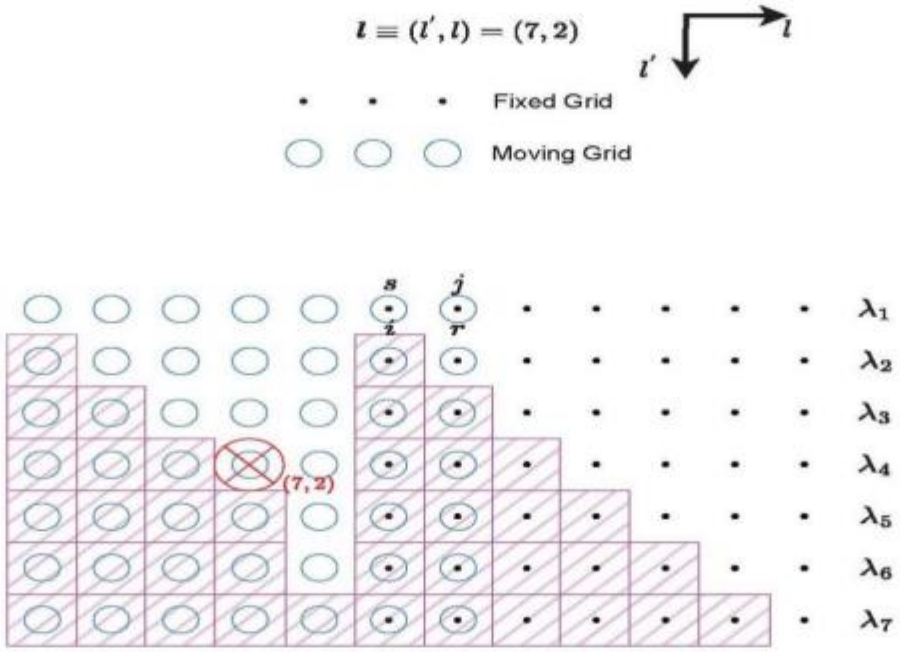

Figure 5 – Optical Transfer Function at spatial frequency coordinate l = (7, 2).

now two columns that are overlapping (the first two columns of the fixed grid and the last two columns in the moving array). This is the so-called 2- point overlap scenario since that, at each wavelength, there are only two points of the entrance pupil plane sampled grid that are overlapping. The WOLF-Iota algorithm is used to solve the 2-point overlap problem in a similar fashion as the WOLF-Tau algorithm is used to solve the 1-point overlap problem illustrated in Figure 4. For the 2-point overlap problem, the Gonsalves error metric shown in Equation (7) works fine and can be directly used as the error metric in the minimization problem, however we will see that this is not necessary since we are using the aperture mask, and a faster way is available to us. By inspecting Figure 5, we see that the OTF and diversity OTF are now being evaluated at one horizontal unit to the right of the previous 1-point overlap case at the new l – grid location (7, 2) illustrated by the red circularly inscribed X. We notice by inspecting Figure 5 that there are three non zero cells contributing to the OTF and diversity OTF. The top-left overlapping cell has complex exponential phase difference $e^{j\Delta\theta_{i,s}^{\lambda 1}}$ where $\Delta\theta_{i,s}^{\lambda 1} = \theta_i^{\lambda 1} - \theta_s^{\lambda 1}$. Recall that the complex exponential phase difference term in this top left-most cell is given by the product of the fixed array GPF with the complex conjugated moving grid GPF. Similarly, the second cell from the top-left fixed array is given by the complex exponential phase difference $e^{j\Delta\theta_{r,j}^{\lambda 1}}$ where $\Delta\theta_{r,j}^{\lambda 1} = \theta_r^{\lambda 1} - \theta_j^{\lambda 1}$. Notice that for this 2-point overlap in the top row of Figure 5 we include the values of $\theta_i^{\lambda 1}$ and $\theta_j^{\lambda 1}$ which were previously determined from our 1-point overlap problem in Figure 4. Consequently, we only have two unknowns $\theta_r^{\lambda 1}$ and $\theta_s^{\lambda 1}$ that need to be estimated to determine the top-row OTF parameters. If we select $\lambda 1$ for filter F1 in the optical layout in Figure 2 to go along with the instantiation of the GPF autocorrelation shown in Figure 5, then the image at detector D1 only has contributions from the top-row of the entrance pupil, since the other wavelength contribution in the second row from the top is filtered out. We can then determine the $\lambda 1$contribution of the irradiance spectrum by taking the 2D Fourier transform of the detected irradiance and looking at the l – grid (7, 2) component for this complex numerical value. In a similar fashion, the diversity image irradiance can be obtained by taking the 2D Fourier transform of the irradiance at detector D2 with the transmissive aperture mask Ma1 set to the same entrance pupil mask pattern as at the SLM, and the filter F1 also set to $\lambda 1$. The diversity irradiance spectrum value can then be determined from the cell entry at larger l – grid coordinate (7, 2). The analytical expressions for the OTF and diversity OTF for the $\lambda 1$ wavelength component are given by inspection of Figure 5 as,

$$\mathcal{H}^{\lambda_1}(l_7, f_2) = \left(e^{j\Delta\theta^{\lambda_1}_{l,s}} + e^{j\Delta\theta^{\lambda_1}_{r,j}}\right)/N_{ep}\,, \tag{11}$$

and,

$$\mathcal{H}^{\lambda_1}_d(l_7, f_2) = \left(e^{j\left(\Delta\theta^{\lambda_1}_{l,s} + \Delta\theta^{\lambda_1}_{d;l,s}\right)} + e^{j\left(\Delta\theta^{\lambda_1}_{r,j} + \Delta\theta^{\lambda_1}_{d;r,j}\right)}\right)/N_{ep}\,. \tag{12}$$

where, $\Delta\theta^{\lambda_1}_{d;l,s} = \theta^{\lambda_1}_{d;l} - \theta^{\lambda_1}_{d;s}$ and $\Delta\theta^{\lambda_1}_{d;r,j} = \theta^{\lambda_1}_{d;r} - \theta^{\lambda_1}_{d;j}$ are pre-determined phase offsets from (in principal) the difference in optical path lengths at detectors D_1 and D_2, or introduced by the *SLM* itself. The WOLF-Tau algorithm can be used along with the measured irradiance spectrum $I^{\lambda_1}(l_7, f_2)$ and diversity irradiance spectrum $I^{\lambda_1}_d(l, f_2)$ values to minimize the error metric $E^{\lambda_1}(l_7, f_2)$ in Equation (9), to find the unknown phase estimates of $\theta^{\lambda_1}_r$ and $\theta^{\lambda_1}_s$.[13, 14] One brute force way to accomplish this minimization is having both $\theta^{\lambda_1}_r$ and $\theta^{\lambda_1}_s$ discretized into N_r and N_s samples across [-π, π) and every possible phase combination is evaluated in the error metric $E^{\lambda_1}(l_7, f_2)$. The smallest error (which is zero in the noise free and perfect estimation case) is kept and provides the best estimate for $\theta^{\lambda_1}_r$ and $\theta^{\lambda_1}_s$. Note that for sufficiently large phase estimate sample points N_r and N_s, the number of possible combinations of $\theta^{\lambda_1}_r$ and $\theta^{\lambda_1}_s$ is N_r x N_s and can be quite large (e.g., for $N_r = N_s = 1000$, there are 1,000,000 different possible combinations of $\theta^{\lambda_1}_r$ and $\theta^{\lambda_1}_s$). Once $\theta^{\lambda_1}_r$ and $\theta^{\lambda_1}_s$ are determined by the WOLF-Tau algorithm, Equation (10) can be used to determine the OTF, diversity OTF, $\theta^{\lambda_n}_r$ and $\theta^{\lambda_n}_s$, at all wavelengths in the HSI system's due to the first and second from the left, and first and second from the right columns of the entrance pupil (i.e., for all wavelengths in the entrance pupil plane columns generating the OTFs for the 2-point overlap). At this point, we have 4 columns of entrance pupil plane recovered phase values (first and second, and the last two columns). The same approach can be taken to solve for the remaining points in the spatial linear array in the top row of Figure 5 using the WOLF algorithm, and noting that for all the remaining points, there will only be two unknown phases for any new increment of the larger ***l*** – grid. Consequently, the WOLF algorithm only needs to solve for two unknown phase values for each new OTF point. The other phase values have been determined by previous entrance pupil plane overlap results. Also notice that for each new OTF point that is solved, we also get two full columns of entrance pupil plane phases. Therefore, we only need to solve for $(N_{ep} + 1)/2$ OTF values to fully map out the entrance pupil plane phases at all wavelengths. For our 7-point linear spatial array at 7 different wavelengths, N_{ep} is 7 (number of samples of the spatial linear array) and so we only need 4 OTF points that need to be calculated to fully determine all phase values in the linear entrance pupil. Further these results can then be scaled to all 7 wavelengths using Equation (10) and the full OTF at every spatial OTF point and at every wavelength can be determined by either directly autocorrelating the GPF, or by using the GPF and Fourier means to determine the full OTF. This allows us to use Equation (1) at λ_1 to perform ATC on the linear array. We can also determine the OTF at any spatial frequency and at any other wavelength component. However, it is interesting to note that even though we have the required OTF and entrance pupil plane phase values at all wavelengths and spatial frequency elements of the linear array, we cannot make individual cell corrections at every entrance pupil plane spatial frequency point for all wavelengths other than for λ_1, because the object radiant emittance spectrum is different at different wavelengths, and without using wavelength filters, we only get the total irradiance spectrum across all wavelengths, not at individual wavelengths from the unfiltered, and non-masked imagery. In other words, for our 7 x 7 example in Figure 5, we need to be able to determine $I^{\lambda_n}(l_7, f_2)$ along with $\mathcal{H}^{\lambda_n}(l, f_2)$ at every overlapping cell block in Figure 5 to accomplish ATC on the entrance pupil plane grid elements themselves. Although not required to recover the ATC object spectrum at all wavelengths, we can do this by employing a selective wavelength filter to isolate the contributions of the spectral irradiance at desired wavelengths. If we turn the SLM on for one integration time ($t_i \sim 1ms$) but set filter F_2 to λ_2, we isolate the second row in Figure (5) and get a two-point overlap problem just like we initially had for the top row with λ_1. If we then turn on the aperture mask and still have the filter F_2 set to λ_2, we have a one-point overlap problem in the λ_2 row that can be solved by the WOLF-Tau algorithm. This is advantageous since the WOLF-Tau algorithm only needs to search over one variable, not two like the WOLF-Iota 2-point overlap algorithm. For the example of 1000 discrete phase estimates in the error minimization/entrance pupil plane phase estimation process, the WOLF-Tau algorithm requires

1000 phase estimates whereas the WOLF-Iota requires 1,000,000. In this case we would have a 3-order of magnitude reduction in computation time by using the 1-point overlap approach over the 2-point overlap approach. Notice that for this situation, the analytical expression for the 1-point overlap at λ_2 is,

$$I^{\lambda_2}(l_7, f_2) = \left|O^{\lambda_2}(l_7, f_2)\right| e^{j\left(\emptyset_o^{\lambda_2}(l, f_2) + \Delta\theta_{r,j}^{\lambda_2}\right)} / N_{ep}\ , \tag{13}$$

and the irradiance spectrum at λ_2 is isolated and obtainable from the 2D Fourier transform of the irradiance at detector D_l. Similar to the previous 1-point overlap scenario, we can recover the object magnitude directly from the measured $I^{\lambda_2}(l_7, f_2)$ and we can use the WOLF-Tau algorithm to solve for $\Delta\theta_{r,j}^{\lambda_2}$. Consequently, we can recover the object radiant emittance phase $\emptyset_o^{\lambda_2}(l_7, f_2)$ and now have the ATC object reconstruction at the second wavelength λ_2. We are also able to determine one of the two unknown entrance pupil plane phases $\theta_r^{\lambda_2}$ directly from the WOLF-Tau algorithm and can determine the entrance pupil plane phases at all other wavelengths in the second column from the left of the fixed array using $\lambda_2\theta_r^{\lambda_2} = \lambda_n\theta_r^{\lambda_n}$. The results for the other unknown entrance pupil plane phase $\theta_s^{\lambda_2}$ can be determined from our measurement of $I^{\lambda_2}(l_7, f_2)$ with the aperture mask turned off and the filter set to λ_2, and substituting in our determined values into Equation (13) and solving for $\theta_s^{\lambda_2}$. This process can be repeated for any desired wavelength using the 1-point overlap procedure at the appropriate wavelength. In this fashion, all entrance pupil plane phases, OTF complex exponential phase difference elements for each overlapping entrance pupil plane grid cell in Figure 5, and object radiant emittance spectrum values for each wavelength and spatial pixel can be determined, thereby allowing an atmospheric turbulence correction at each spatial frequency element/OTF location for all wavelengths. These corrections only require the faster WOLF-Tau (1-point overlap) algorithm and, after the first top-left cell is determined producing estimates of $\theta_i^{\lambda_1}$ and $\theta_j^{\lambda_1}$, the rest of the 1-point overlap solutions can in principle be determined independently from one another and in parallel. However, the parallel implementation is not practical with the conceptual layout shown in Figure 2 since only two filtered images can be collected at a time and the HSI system may have hundreds of different wavelengths. With the layout shown in Figure 2, only a few significant wavelengths can be corrected at a time with the approach above since the overall correction depends on the atmosphere being relatively constant from Taylor's frozen flow approximation. We can develop a general equation for the analytical expression of the irradiance spectrum of the 1-point overlap scenario at any wavelength by first defining some useful notational conventions. If we define in general that $\theta_r^{\lambda_n}$ at the wavelength λ_n under consideration is the entrance pupil plane phase that is always one point to the right of the first point of the fixed array (i.e., one point to the right of $\theta_i^{\lambda_n}$), and that $\theta_s^{\lambda_n}$ is always the point to the left of the last point of the moving array (i.e., one point to the left of $\theta_j^{\lambda_n}$), then the two unknown phases will always be $\theta_r^{\lambda_n}$ and $\theta_s^{\lambda_n}$ for any filtered 1-point overlap problem at any wavelength in Figure 5. Also, the second phase in the 1-point overlap complex exponential OTF expression will always be $\theta_j^{\lambda_n}$. By using this convention along with our convention for $\theta_i^{\lambda_n}$ and $\theta_j^{\lambda_n}$ from before, we can write the analytical expression for the irradiance spectrum at spatial frequency coordinate f_n and the entrance pupil plane mask on, and filter λ_n on as,

$$I_{on}^{\lambda_n}\left(l_{N_{ep}}, f_n\right) = \left|O^{\lambda_n}\left(l_{N_{ep}}, f_n\right)\right| e^{j\left(\emptyset_o^{\lambda_n}\left(l_{N_{ep}}, f_n\right)\right)} \left[\frac{e^{j\Delta\theta_{r,j}^{\lambda_n}}}{N_{ep}}\right], \tag{14}$$

where $l_{N_{ep}}$ represents the vertical $l-$ grid midpoint of the autocorrelation of the GPF (in this case in the direction of wavelengths). We can use the WOLF-Tau algorithm to determine $\theta_r^{\lambda_n}$, and the object radiant emittance spectrum can be determined directly by taking the magnitude of Equation (14). If we now capture the image with the mask turned off and filter F_2 turned on at λ_n, we get the following analytical result,

$$I_{off}^{\lambda_n}\left(l_{N_{ep}}, f_n\right) = \left|O^{\lambda_n}\left(l_{N_{ep}}, f_n\right)\right| e^{j\left(\emptyset_o^{\lambda_n}\left(l_{N_{ep}}, f_n\right)\right)} \left[\frac{e^{j\left(\Delta\theta_{i,s}^{\lambda_n}\right)} + C^{\lambda_n} + e^{j\left(\Delta\theta_{r,j}^{\lambda_n}\right)}}{N_{ep}}\right] \tag{15}$$

where the complex constant at λ_n is determinable from the sums of previously determined complex exponential phase differences between the first and last elements of overlapping entrance pupil plane grid points on row λ_n, such as is shown in Figure 5. Note that C^{λ_n} is non-zero only for overlaps greater than or equal to three. For the λ_2 row, C^{λ_2} is equal to zero, and for the λ_1 row, there is only one complex exponential phase difference term for the OTF that has a phase difference of $\theta_{i,j}^{\lambda_n}$. Once $\theta_r^{\lambda_n}$ is determined using the WOLF-Tau algorithm from Equation (14), we can solve for $\theta_s^{\lambda_n}$ directly from Equation (15) by dividing one equation by the other and solving for the only remaining unknown, $\theta_s^{\lambda_n}$. Subsequently, we can use Equation (15) to determine the OTF at λ_n.

$$\mathcal{H}^{\lambda_n}\left(l_{N_{ep}}, f_n\right) = \left[\frac{e^{j\left(\Delta\theta_{i,s}^{\lambda_n}\right)} + C^{\lambda_n} + e^{j\left(\Delta\theta_{r,j}^{\lambda_n}\right)}}{N_{ep}}\right]. \tag{16}$$

With Equation (16), we can now determine the ATC corrected imagery at every point of the HSI push broom sensor and at every HSI wavelength. Once this is accomplished, the platform motion advances the row of spatial pixels at λ_1, over time t_p to the next row of the image frame, and the ATC process described above is repeated to generate the second row of the integrated image over all the HSI wavelengths. This means that all the wavelength filtering that needs to occur must be accomplished within the time t_p it takes the HSI platform to advance the push broom sensor one row, or store the required image set (irradiance and diversity irradiance for the following cases (mask on, filter on; mask off filter on) for each of the required $(N_{ep} + 1)/2$ wavelengths, or store this information on the platform for later processing. Alternatively, the general WOLF methodology that includes all the sub-algorithms for the 1-point, 2-point, and 3-point (or more) scenarios can be used to correct the entire row of one of the wavelengths using only the simultaneously captured image irradiance spectrum and diversity image spectrum for that row, and these results could be scaled to the other wavelengths of the HSI system. No aperture mask is required for this method and fewer data sets are needed (only the irradiance spectrum and diversity irradiance spectrum at each wavelength with no aperture mask). However, we would lose the potential speed increase (almost 3 orders of magnitude at 1000 entrance pupil plane phase sample points) in restricting the WOLF solver to only use its fastest algorithm (the 1-point overlap WOLF-Tau algorithm). This direct, but slower, WOLF approach can also be used for any of the implementation approaches shown in Figure (1), such as the non-scanning HSI cube shown at the top-right of the figure. As an example, on the left side of Figure 6, we see a collection of HSI landscape imagery arranged in a hypercube. On the right side of Figure 6 we have one spatial slice of the hypercube data (2D

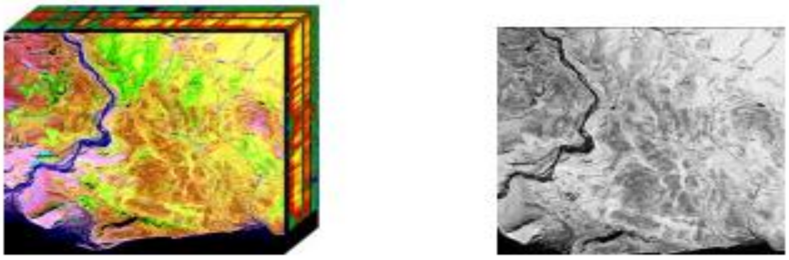

Figure 6 – Hyperspectral Imaging System data hypercube (left) and response at one wavelength (right). Courtesy of Dr. Nicholas M. Short, Sr. - NASA http://rst.gsfc.nasa.gov/, Public Domain, https://commons.wikimedia.org/w/index.php?curid=25442380

spatial data at one wavelength) that serves as our reference (truth) image. We apply strong simulated atmospheric turbulence to the reference image at λ_1 shown on the right side of Figure 6 and apply a Von Karman atmospheric turbulence model that has the correct atmospheric turbulence statistics and is useful for modeling strong atmospheric turbulence in high wind conditions. Figure 7 shows the atmospheric turbulence degraded image for the reference single wavelength HSI image irradiance (left), and the associated diversity image Irradiance (middle). On the right side of Figure 7, we see the WOLF ATC corrected image

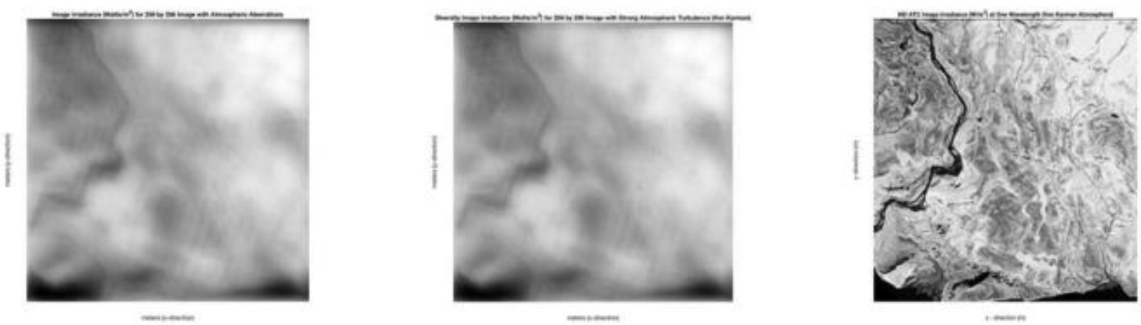

Figure 7 – Simulated atmospheric turbulence degraded HSI image irradiance at one wavelength (left), atmospheric turbulence degraded diversity irradiance (middle), ATC irradiance using the WOLF methodology (right).

at $\lambda 1$ as applied to these two simulated atmospheric turbulence-degraded images. This ATC corrected image has 127 by 127 entrance pupil plane samples at one wavelength. This would be the equivalent of one wavelength slice of 253 rows of an HSI push broom imaging system with 253 pixels. There would be 253 by 253 OTF values associated with the 2D spatial frequency elements of the image at a single wavelength of the HSI hypercube. Each vertical slice of the HSI hyper cube would have an entrance pupil plane array with 127 vertical wavelengths and 127 spatial irradiance spectrum pixels (and simultaneously a similar slice for the diversity irradiance spectrum pixels at all wavelengths). This slice of the hyperspectral cube requires the WOLF-Tau algorithm to be solved at 64 wavelengths to fully map out the entrance pupil plane phases at all HSI wavelengths, and determine the ATC corrected imagery at all wavelengths for that slice. From complexity analysis studies, it has been shown that the current WOLF algorithm implementation can perform ATC on a 256 by 256 image segment (with associated diversity image segment) in approximately 9 seconds on conventional computational platforms such as laptop computers.[8] This number has been confirmed using a 2014 non-optimized MacBook Pro laptop computer running Matlab without any parallel processing hardware support. By employing the aperture mask approach described above, a three order of magnitude improvement in this processing time would conceptually be possible and place the single wavelength spatial ATC correction for the hypercube at around 9 ms, without parallel processing technology, provided the data I/O doesn't bottle-neck the processor. Figure 8 shows a comparison of the WOLF methodology (with and without the aperture mask approach described above) and traditional correlation and Fourier-based ATC methods as a function of number of camera pixels in a linear direction (e.g., the actual camera pixels on a square detector is the square of the number of pixels shown on the horizontal axis of Figure 8. The top figure in red shows the number of elementary operations required by a representative traditional correlation-based ATC method as a function of number of camera pixels in a linear direction. The second from the top (green) result shows the number of elementary operations for a traditional Fourier-based phase diversity ATC implementation. The third from the top shows the number of estimated elementary operations for the original WOLF methodology without any optimizations or parallel processing implementations, and the bottom (black) line represents the projected performance in elementary operations of the WOLF methodology using the entrance pupil plane aperture mask as discussed above. The elementary operations were estimated by breaking down representative ATC algorithms into the fundamental numbers of adds, subtracts, multiplies, and divides in the algorithms and subsequently scaled to the number of camera pixels processed in a square camera array of various pixel sizes. These results were cross checked by applying complexity analysis methods to the WOLF results, and then checking the complexity analysis results through simulation over multiple laptop computers spanning the years from 2014 until 2021.[8] Good agreement was seen between the elementary operations approach, complexity analysis results, and our simulations. Some other important technical performance metrics (TPMs) for the WOLF algorithm include the ratio of entrance pupil plane

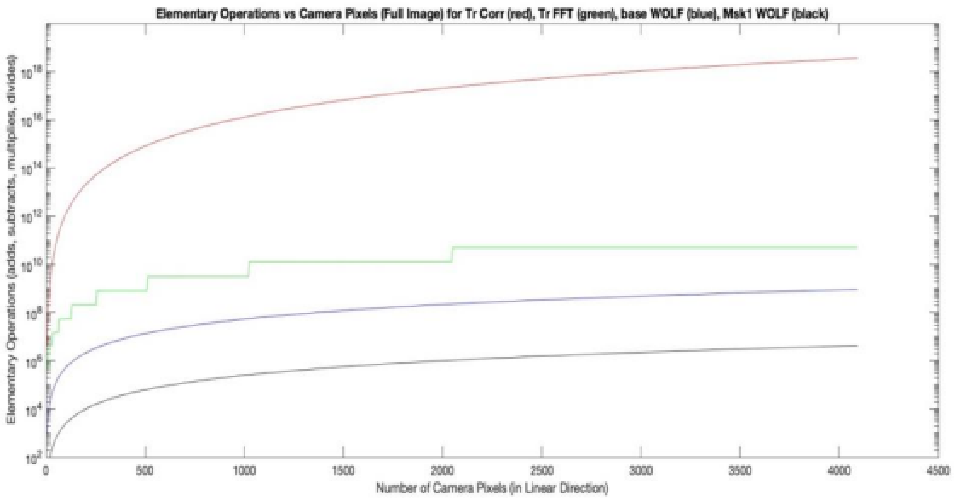

Figure 7 – Number of elementary operations for representative traditional correlation-based ATC methods (top, red), traditional Fourier based methods (second from top, green), base WOLF with no optimization or parallelization (third from top, blue), and WOLF method with aperture mask (bottom, black).

diameter to the atmospheric coherence length (Fried parameter) r_o.[17] The larger the value this is, the better the spatial resolution increase obtained by removing the atmospheric turbulence. Also, if this ratio is 1 or less, then there will be no improvement in the spatial resolution of the image by removing the atmospheric turbulence.

SUMMARY Using the method leading up to Equations (14) and (15), we have shown a conceptual framework for using the WOLF methodology to quickly produce ATC spatial imagery and shown that the corrections at one wavelength can readily be extrapolated to correct imagery at all other wavelengths of a push broom HSI imaging system. Since it is possible in principle to correct the spatial imagery across all wavelengths, the per pixel signal-to-noise ratio at the detector output can be increased at all wavelengths where there is a detectable amount of signal, and so wavelength dependent discrimination is consequently also improved. For the case of an HSI push broom sensor system, a conceptual model was presented that has the potential for dramatically improving the ATC computational speed at the price of some hardware complexity (i.e., the use of a selectable spatial light modulator and/or aperture masks, dual optical paths with selectable optical path difference hardware, prisms, and selectable wavelength narrow-band filters). The SLM can also be used to imprint a priori phase differences on the entrance pupil irradiance spectrum to create the required diversity image for the WOLF methodology thereby eliminating the need for the OPD adjustment in the second leg of the conceptual layout in Figure 2. The SLM can also be used to implement corrections to the imagery once the entrance pupil plane phases have been determined at all wavelengths. The computational speed improvement in the conceptual layout in Figure 2 is approximately 3 orders of magnitude faster than the current WOLF implementation for 1000 discrete entrance pupil plane phase estimates in the WOLF's error minimization algorithm. The WOLF methodology in its current configuration can be directly applied to any of the types of HSI systems shown in Figure 1 without any of the additional hardware in the conceptual model, except for the requirement of simultaneously capturing both the irradiance and diversity irradiance. However, the current WOLF implementation is computationally slower than the aperture masked approach outlined in this paper. As a point of reference, the current WOLF algorithm can perform ATC of a 256 by 256 pixel image in approximately 9 seconds with no parallel processing, or optimization on a 2014 MacBook Pro running in MatlbTM. [8] This measured time is consistent with complexity analysis results of the WOLF algorithm.[17] An approximate three order of magnitude improvement over the current WOLF implementation may be achieved by using the mask-based conceptual approach outlined above with the fast WOLF-Tau 1- point overlap algorithm. Parallel processing hardware can also be used to simultaneously evaluate the error metric used within the WOLF algorithm itself providing a proportional computational speed increase based on the number of simultaneously processed phase values estimated in the core error metric calculations of the WOLF algorithm, barring I/O overhead, memory access, and data piping issues.

REFERENCES

1. Hardy, J. W. "Adaptive Optics for Astronomical Telescopes." Oxford University Press, 1998.
2. David L Fried. Optical heterodyne detection of an atmospherically distorted signal wave front. Proceedings of the IEEE, 55(1): 57–77, 1967.
3. Hubin, N., Ellerbroek, B., et. al., "Adaptive Optics for Extremely Large Telescopes: An Introduction," Proceedings of the International Astronomical Union, VOL. 1, (1 November 2006).
4. M. C. Roggemann, B. Welsh, Imaging Through Turbulence, CRC Press, New York, 1996.
5. Glenn A. Tyler "Adaptive optics compensation for propagation through deep turbulence: a study of some interesting approaches," Optical Engineering 52(2), 021011 (15 November 2012).
6. William W Arrasmith. High-speed diversity-based imaging method for parallel atmospheric turbulence compensation, May 21, 2013. US Patent 8,447,129.
7. W. Arrasmith. "Diversity-based atmospheric turbulence compensation for incoherent imaging systems using a new well optimized linear finder methodology," Universal Journal of Lasers, Optics, Photonics & Sensors, Vol. 2 Issue No. 1 – June 2021.
8. Xin, Yang, William W. Arrasmith, and Erlin He. "Order analysis comparison between traditional fourier transform-based atmospheric turbulence compensation methods and new well optimized linear finder methodology," Universal Journal of Lasers, Optics, Photonics & Sensors, Vol. 2 Issue No. 1 – June 2021.

9. File: Multispectral acquisition techniques.svg," Wikimedia Commons, the free media repository. https://upload.wikimedia.org/wikipedia/commons/b/b8/Multispectral_acquisition_techniques.svg
10. Willett RM, Duarte MF, Davenport MA, Baraniuk RG (2014) Sparsity and Structure in Hyperspectral Imaging Sensing, Reconstruction, and Target Detection. IEEE Signal Process. Mag. 31(1), 116–126. 10.1109/MSP.2013.2279507.
11. Schott, John R. Remote sensing: the image chain approach. Oxford University Press on Demand, 2007.
12. Gaskill, Jack D. Linear systems, Fourier transforms, and optics. Vol. 56. John Wiley & Sons, 1978.
13. Goodman, Joseph W. Introduction to Fourier optics. Roberts and Company publishers, 2005.
14. RA Gonsalves. Phase retrieval from modulus data. JOSA, 66(9):961–964, 1976.
15. Robert A Gonsalves. Phase retrieval and diversity in adaptive optics. Optical Engineering, 21(5):215829, 1982.
16. Robert A Gonsalves and Robert Chidlaw. Wavefront sensing by phase retrieval. In Applications of Digital Image Processing III, volume 207, pages 32–39. International Society for Optics and Photonics, 1979.
17. Beckers, Jacques M. "Adaptive optics for astronomy: principles, performance, and applications." Annual review of astronomy and astrophysics 31.1 (1993): 13-62